Chapter-3

$NiC_2O_4 \cdot 2H_2O$ Nanoflakes: A Novel Redox mediated Intercalative Pseudocapacitive Electrode for Supercapacitor Applications

3.1 Introduction:

Several transition metal-oxides such as MnO_2, Nb_2O_5, and RuO_2 are explored as electrodes for pseudocapacitor applications.[1,2] Due to its open-pore framework structure and more structural stability, Transition metal oxalates have been explored as potential energy storage materials partly because of the planar oxalate anions ($C_2O_4^{2-}$) network.[3-4] Hydrated Transition metal oxalates in general show a more open framework structure through a 3-dimensional hydrogen bonding network as compared to anhydrous Transition metal oxalates. Further, Transition metal oxalate-based supercapacitors perform better in aqueous electrolytes as compared to non-aqueous electrolytes. Aqueous electrolytes have significant inherent advantages over non-aqueous electrolytes as they are cheap, safe, and has twice ionic conductivity as compared to the non-aqueous electrolyte.[5-6]

In this work, we have envisaged hydrated $NiC_2O_4•2H_2O$ as an electrode in an aqueous KOH and neutral Na_2SO_4 electrolyte for pseudocapacitive energy storage applications. $NiC_2O_4•2H_2O$ nanoflakes were synthesized by the single-step co-precipitation method at room temperature. Superior specific capacitance equivalent to 990 F/g for $NiC_2O_4•2H_2O$ electrode in the potential window of 0 to 0.45 V was observed in an aqueous 2M KOH electrolyte. Specific capacitance equivalent to 440F/g in neutral 1M Na_2SO_4 electrolyte in the operating window of 0 to 0.85 V was also observed for $NiC_2O_4•2H_2O$ electrodes. Further, we assembled an aqueous asymmetric supercapacitor (AAS) in which $NiC_2O_4•2H_2O$ is made as a positive electrode and Activated Carbon (AC) as the negative electrode. A maximum energy density of 141.5 Wh/kg and specific power density of 5554 W/kg were obtained at 0.2 A/g current density, by the combination of $NiC_2O_4•2H_2O$ and AC full cell with high cyclic stability. Synthesis, characterizations, and detailed electrochemical studies of the developed $NiC_2O_4•2H_2O$ nanoflakes electrode are presented in the manuscript.

3.2 Experimental

3.2.1 Synthesis

For the synthesis of $NiC_2O_4•2H_2O$, 5.94g (0.1 M) of Nickel (II) nitrate hexahydrate ($Ni(NO_3)_2.6H_2O$) was dissolved in 200 ml of deionized water with continuous stirring at a hot plate magnetic stirrer and 2.54g (0.1 M) oxalic acid dihydrate ($H_2C_2O_4.2H_2O$) were added in the required solution. The entire mixture was stirred vigorously at 80°C for 3 h. After 3 h of stirring green color precipitate of product $NiC_2O_4•2H_2O$ was obtained. The obtained product is then washed several times with deionized water. Finally, the washed products were dried in a hot air oven at 100°C for 12 h. The product formation is presented in equation3.1.

$$Ni(NO_3)_2.6H_2O + H_2C_2O_4.2H_2O \rightarrow NiC_2O_4•2H_2O + 2HNO_3 + 6H_2O \quad (3.1).$$

3.2.2 Characterizations

The phase purity and structure of the material were examined through RigakuMiniflex desktop X-ray Diffractometer (XRD) with Cu-Ka radiation (λ= 0.154nm) in the range 2θ = 10º–90º with a step size of 0.02º. Xpert High Score (PANanylytical) software was used to identify the required phase. FE-SEM (FP 5022/22) was used to determine the surface morphology and structure of the sample. Infrared spectra of the samples were recorded using the Nicolet iS5 FTIR spectrometer in the range of 400 to 4000 cm^{-1}. Pore size distribution and specific surface area of the sample were measured by BET (MicrotracBEL). All electrochemical performances of the sample including cyclic-voltammetry (CV), galvanostatic charge-discharge GCD, and Electrochemical Impedance Spectroscopy (EIS) was conducted using a conventional three-electrode arrangement and were measured by Metrohm Autolab (PGSTAT204) equipped with the FRA32M module. Electrochemical measurements were analyzed using NOVA1.1 software.

3.2.3 Preparation of Electrode

Working electrodes were prepared by taking the required amount of active material, activated carbon, and Polyvinylidene difluoride (PVDF) binder in the ratio of 7:2:1 ratio in N-Methyl-2-Pyrrolidone (**NMP**) solvent. To prepare the working electrode, the homogeneous viscous slurry was prepared in mortar and pestle accompanied by casting over a 1cm^2 area of Toray carbon paper. Further, the coated electrode was dried at 80^oC for 12 h. Activated carbon was utilized to increase the conductivity of electrodes in electrode preparation. The electrode loading was calculated by taking the weight of the electrode on an electronic balance (error limit: 0.01mg). For that, the first weight of Torrey paper was taken then the weight of coated electrode (after drying the coated ink on Torrey carbon paper on a 1x1 cm^2 area). Then from the difference in the weight, the exact loading of electrode material was calculated. Typically, the total electrode load was taken 1 mg (0.7 mg active material: activated carbon: PVDF binder).

3.3 Results and Discussions

3.3.1 XRD Study

XRD was used to examine the overall crystallinity and phase purity of synthesized $NiC_2O_4•2H_2O$. Figure 3.1 shows the XRD pattern of the prepared sample of $NiC_2O_4•2H_2O$ over the range of 2θ range of 10-60° with a step size of 0.02º. The prominent sharp diffraction peak matches with JCPDS file: 001-0299, confirming the high crystallinity of $NiC_2O_4•2H_2O$ and is indexed to the β-orthorhombic phase of $NiC_2O_4•2H_2O$ having space group *Cccm* with lattice parameters a = 11.842 Å, b = 5.345 Å and c = 15.716 Å.[7-8] The crystallite size was calculated by using the Debye-Scherrer equation and the calculated value was found to be ~20(±2) nm.

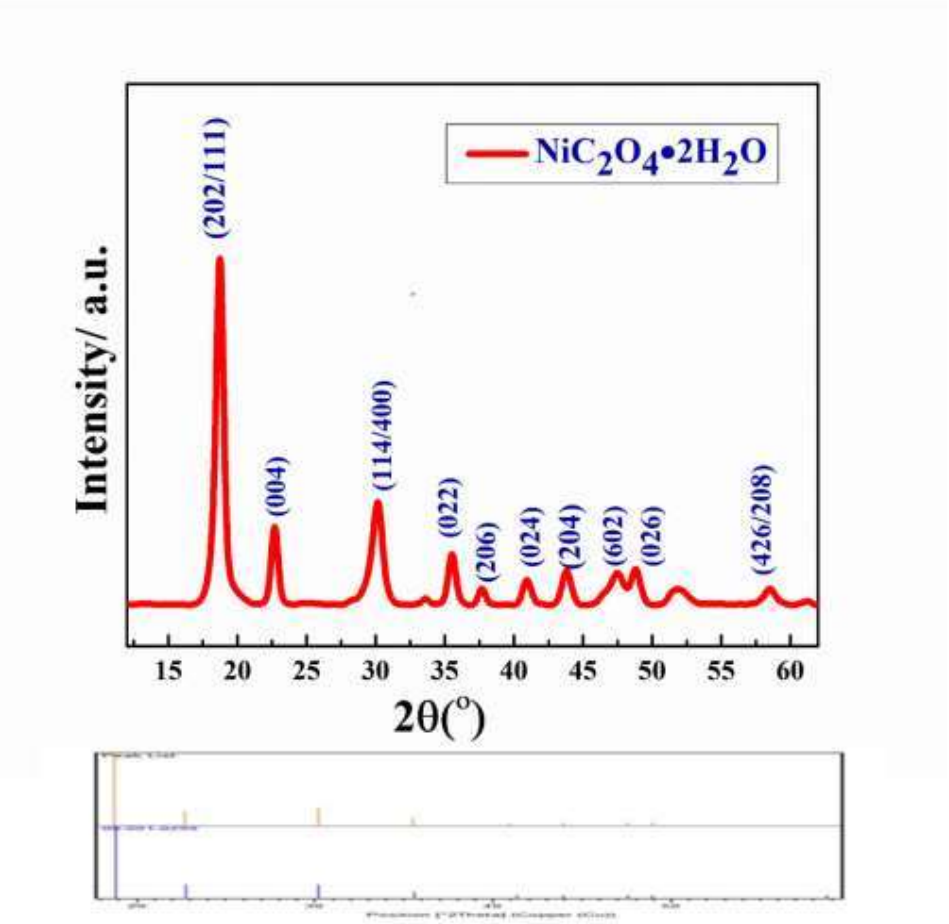

Figure 3.1: Powder XRD of the prepared sample of $NiC_2O_4•2H_2O$.

3.3.2 SEM/EDX Study

The SEM image is shown in Figure 3.2(a) displays particle size distribution and flake type morphology of $NiC_2O_4•2H_2O$ powder. Prepared $NiC_2O_4•2H_2O$ consists of 200–1000 nm range particles exhibiting uniform polyhedral flakes type morphology. Figure 3.2(b) shows the EDX (energy dispersive x-ray) analysis image confirming the composition of the material. Figure 3.2(c) shows the HRTEM image and 3.2(d) lattice fringes of nanoflakes type $NiC_2O_4•2H_2O$ sample. Inset (i, ii, and iii) of 3.2(d) show FFT image, enlarged lattice fringes, and d-spacing of nanoflakes type $NiC_2O_4•2H_2O$ sample. The calculated d spacing value was found to be 0.239 nm, which matches with the (202) plane of the $NiC_2O_4•2H_2O$ sample.

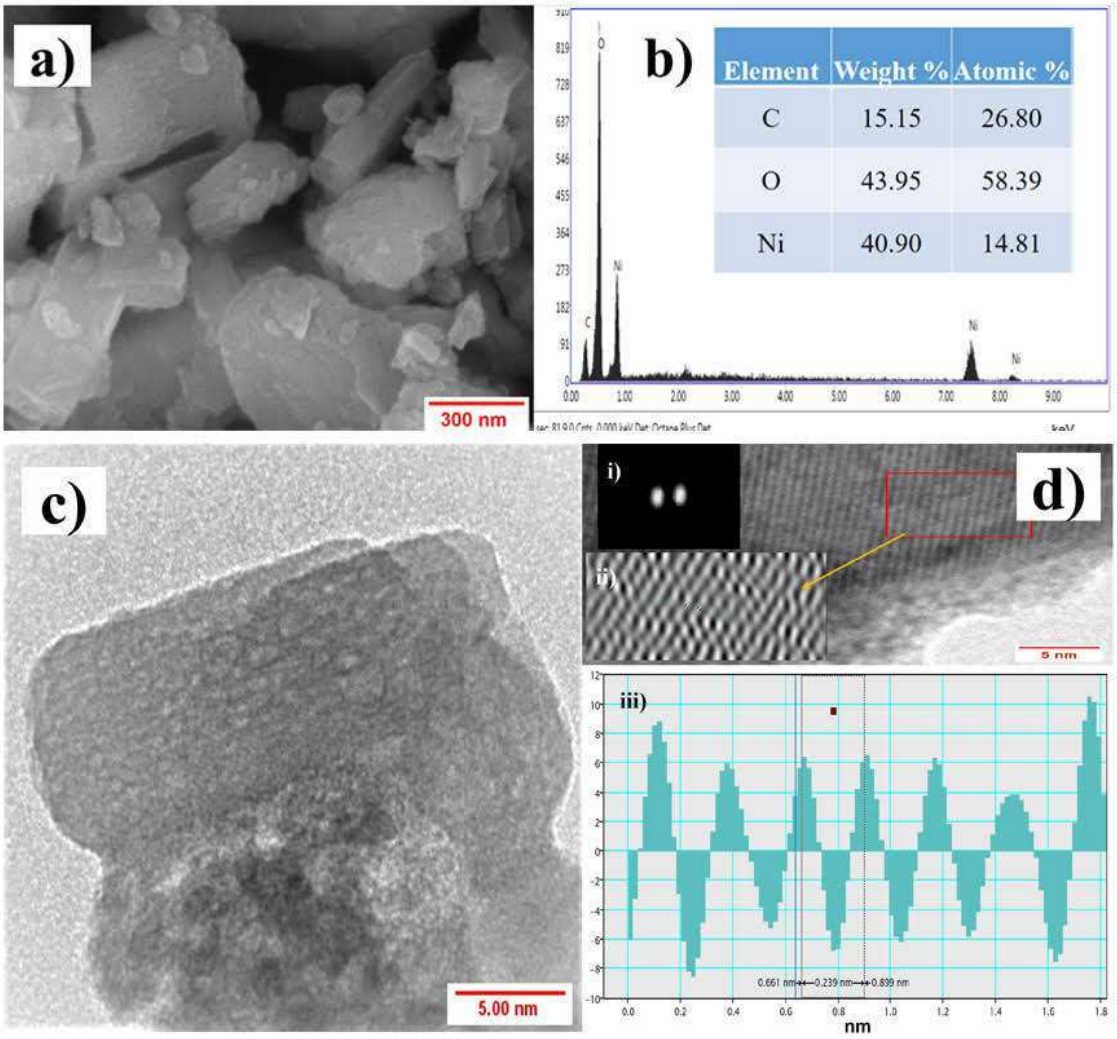

Figure 3.2. (a) FE-SEM images and (b) EDX analysis image of the prepared sample of $NiC_2O_4•2H_2O$ sample showing flake type morphology. (c) HRTEM and (d) lattice fringes of nanoflakes type $NiC_2O_4•2H_2O$ sample. Inset (i, ii, and iii) of (d) show FFT image, enlarged lattice fringes, and d-spacing of nanoflakes type $NiC_2O_4•2H_2O$ sample.

3.3.3 Thermal Analysis

Thermogravimetric analysis (TGA) as shown in Figure 3.3 was used for qualitative analysis of $NiC_2O_4•2H_2O$ in the N_2 atmosphere. First weight loss occurred from 120ºC-300ºC, which corresponds to the removal of hydrated water from the sample. TGA curve at 220 ºC, determines the weight loss of 22.489% equivalent to 2 moles of water loss from the sample. Similarly, the second weight loss step occurs at the temperature range of 350–500ºC in which

a weight loss of 40.190% was observed. During the second step, CO and CO_2 were released into the atmosphere accompanied by the formation of NiO as the final product.[10] The weight losses that appeared in the TGA study are represented by equation 3.2&3.3:

$$NiC_2O_4 \cdot 2H_2O \rightarrow NiC_2O_4 + 2H_2O \quad (T\sim 200^oC) \qquad (3.2)$$

$$NiC_2O_4 \rightarrow NiO + CO + CO_2 \quad (T\sim 450^oC) \qquad (3.3).$$

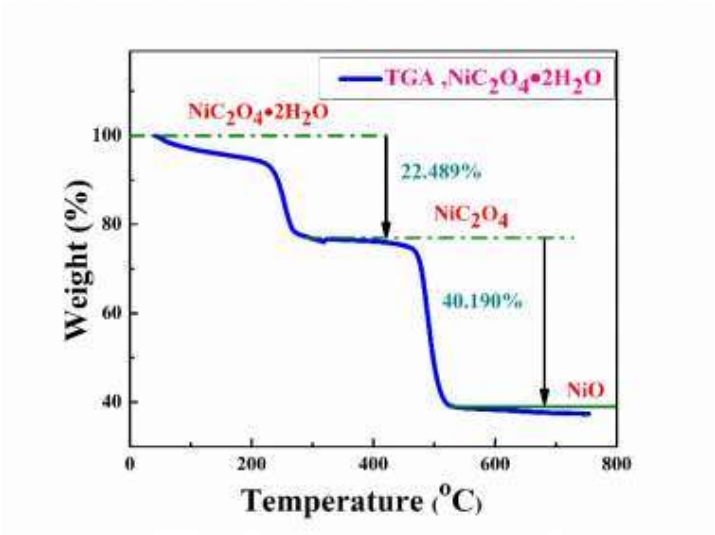

Figure 3.3: TGA of $NiC_2O_4 \cdot 2H_2O$ in N_2 atmosphere.

FTIR spectrum of $NiC_2O_4 \cdot 2H_2O$ powder shown in Figure.3.4 reveals the presence of different functional groups at different wavenumber (cm^{-1}).[8-10] The broad peak at 3400 cm^{-1} ascribed to the stretching vibration of a hydroxyl group (ν (-OH)) signifies the presence of water in the compound. The observed peak at 1626 cm^{-1} was assigned for anti-symmetric carbonyl stretching band *vs*(C=O) specific to the oxalate group.[10] Two weak peaks at 1359 cm^{-1} and 1317 cm^{-1} were attributed to vibrations of $C_2O_4^{-2}$ *vs*(C–O) + *v*(C–C) and *vs*(C–O) + δ(O–C=O), respectively. The peak at 829 cm^{-1} was assigned to the vibration mode of $C2O4^{-2}$, O–C=O bending vibrations (δ(O–C=O)). The absorption peak at 490 cm^{-1} can be attributed to Ni–O bonding present in prepared samples of $NiC_2O_4 \cdot 2H_2O$.

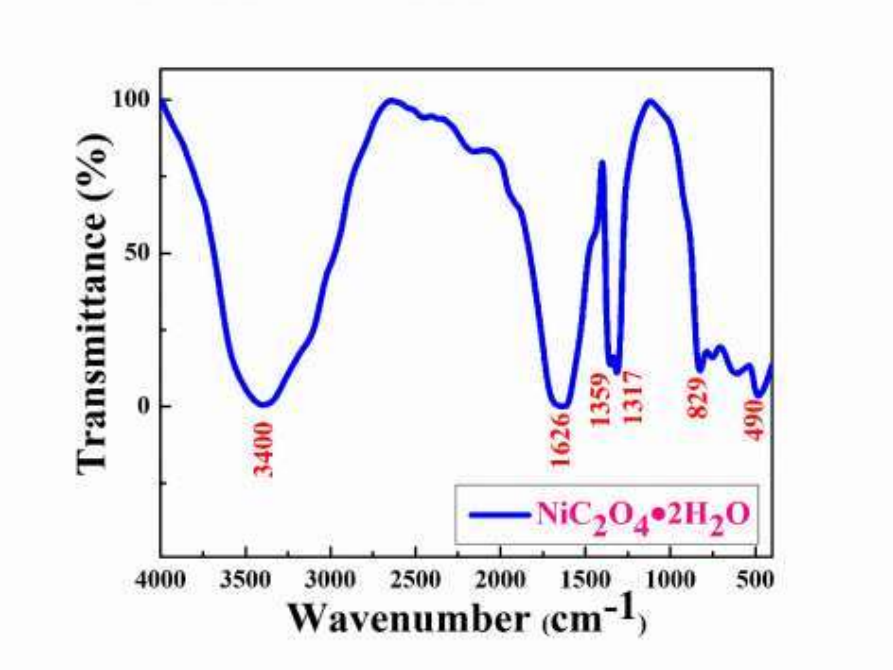

Figure 3.4: FTIR of $NiC_2O_4•2H_2O$ sample.

Figure.3.5 represents the BET surface area measurements result of the $NiC_2O_4•2H_2O$ sample. The nitrogen adsorption and desorption isotherm show type IV characteristics which is corresponding to a complex mixture of micro and mesoporous structure for the $NiC_2O_4•2H_2O$ sample. The calculated BET-specific surface area and average pore diameter are 22.9 m^2/g and 3.75 nm, respectively. Fast diffusion of ions into mesopores structures attributes to excellent electrochemical performances.[11] The calculated mesopores diameter of the $NiC_2O_4•2H_2O$ sample is much bigger than the OH^- ions present in an aqueous KOH electrolyte.[12]

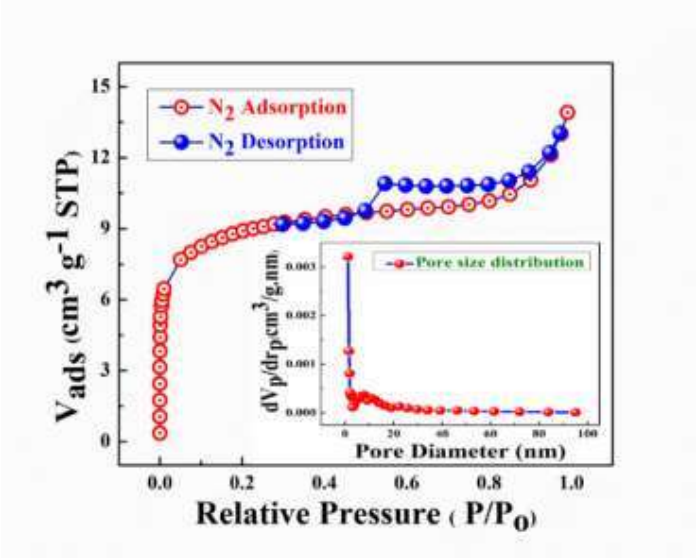

Figure 3.5: BET nitrogen adsorption/desorption isotherm of $NiC2O_4•2H_2O$ sample.

3.3.4 Electrochemical Studies

The electrochemical performance of $NiC_2O_4•2H_2O$ as a working electrode was characterized using a three-electrode system where $NiC_2O_4•2H_2O$ was employed as a working electrode, saturated calomel electrode (SCE) as a reference electrode, and Platinum electrode as counter electrode in 2M KOH as an electrolyte. The charge storage behavior of $NiC_2O_4•2H_2O$ was characterized by using cyclic voltammetry (CV) experiment. The CV curve is shown in Figure 3.6(a) depicts the presence of one pair of well-separated redox peaks at +0.38/+0.21 V. These peaks originated due to the reversible transformation between Ni^{2+} to Ni^{3+} as represented in equation 3.4.

$$Ni^{2+}C_2O_4•2H_2O + OH^-_{sol} \leftrightarrow (Ni^{3+}OH^-)C_2O_4•2H_2O + e^- \quad (3.4)$$

From the CV curve, the specific capacitance C (F/g) can also be calculated as one of the significant parameters to understand the electrochemical performance of the working electrode. [13-14]The formula for the calculation of specific capacitance is given in equation 3.5.

$$Csp = \frac{\int i\,(V)dV}{2mV\vartheta} \quad (3.5)$$

where 'm' is the mass of active material in the electrode (g), 'V' is the potential window (V) and 'ϑ' is the scan rate (mV/s). The CV curves at different scan rates ranging from 0.5 to 10mV/s are shown in Figure 3.6(b). The specific capacitances from the cyclic-voltammetry curve were calculated using equation 3.5 and capacitance was found close to 990 F/g, 910 F/g, 871 F/g, 842 F/g, 778 F/g, and 655 F/g at scan rates of 0.5, 1, 2, 4, 5 and 10 mV/s respectively. With an increasing scan rate, the specific capacitance decreases because at a lower scan rate active sites of the electrode are more accessible for electrochemical reaction.[15] Simultaneously, shifting of anodic peak potential to a more positive and cathodic peak potential to a more negative position was observed with increasing scan rates. Figure 3.6(c) shows the linear relation between anodic and cathodic peak current with respect to the square root of scan rate, indicating that the cyclic-voltammetry curve exhibits a semi-infinite diffusion-controlled process in the electrode. Furthermore, the diffusion kinetics of electrodes can be understood by determining the diffusion coefficient.[16] The diffusion coefficient for the electrode was determined using the Randles–Ševčík equation as represented in equation 3.6.[17-18]

$$i_p = 2.686 \times 10^5 \times n^{3/2} A D^{1/2} C_o v^{1/2} \quad (3.6)$$

Where i_p is peak current (A), n is the number of electrons transferred in the redox event (usually 1), A is electrode area in cm^2, D is diffusion coefficient in cm^2/s, C_o is OH^- ion concentration in mol/cm^3, ν is scan rate in V/s. The diffusion coefficient of diffusion of hydroxide (OH^-) ions was found to be 2.601×10^{-7} cm^2/s for oxidation and 0.975×10^{-7} cm^2/s for reduction respectively for the $NiC_2O_4\cdot2H_2O$ electrode.

To further understand the electrochemical kinetics of charge storage behavior of electrodes in aqueous electrolytes, the power-law presented in equation 3.7 was used.[15, 19]

$$i = a\nu^b \quad (3.7)$$

where a and b are adjustable values, i is the current (A), and ν is the scan rate (V/s). The value of b lies between 0.5 to 1, b = 0.5 stands for the semi-infinite diffusion control reaction for battery-type material while b = 1 stands for the capacitive control reaction.[20] From Figure 3.6(d) and (e), the slopes of the corresponding log (v) versus log (i) plots for anodic and cathodic peaks are found to be 0.68 and 0.70, respectively, consistent with kinetics dominated by the Faradaic intercalation process. [21] Additionally, the amount of charge stored in the outer and inner surfaces was calculated using the Trasatti plot. [22] Generally, the total amount q_t of the charge stored in the electrode is due to the sum of the charge storage contribution from the inner q_i and outer q_o $t\square e$ surface of the electrode as given in equation 3.8.

$$q_t = q_i + q_o \qquad (3.8)$$

Where q_t, q_i and q_o are in C/g. Graphs are shown in Figures 3.6 (e) and (f), plotted between q_o vs. $\nu^{-1/2}$ and q_t vs. $\nu^{1/2}$ and were used to evaluate outer surface charge storage contributions and the total amount of charge stored in the cyclic-voltammetry curve of the electrodes. The calculated value of q_t for the sample electrode was found to be 512 F/g. The specifically calculated values of q_i and q_o for the electrode were found to be 428 C/g and 84 C/g respectively. This confirms that 84% of the charge stored in $NiC_2O_4{\bullet}2H_2O$ electrodes was due to pseudocapacitive intercalation type behavior. Overall it can be inferred that the intercalative pseudocapacitive charge storage mechanism is more dominant for storing the charge at $NiC_2O_4{\bullet}2H_2O$ electrodes.

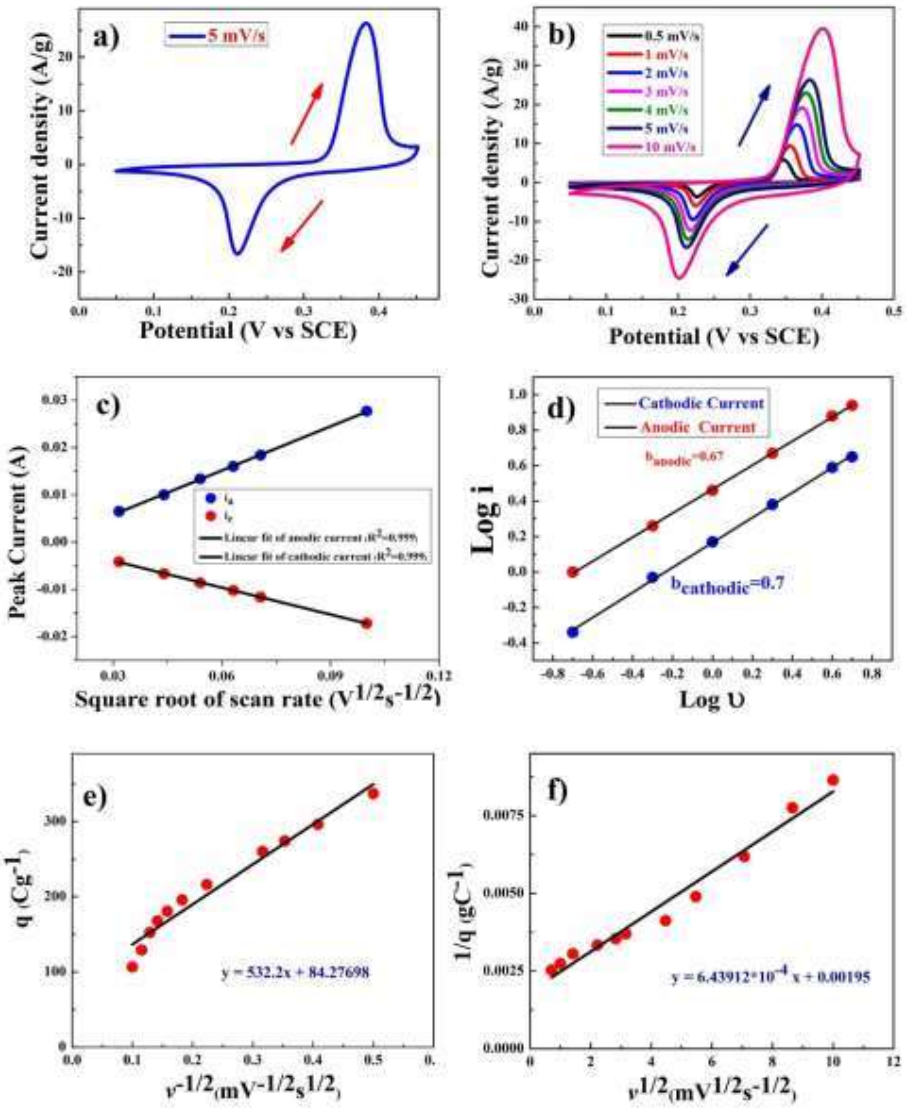

Figure 3.6: (a) CV of $NiC_2O_4 \cdot 2H_2O$ electrode at 5mV/s, (b) CV curves plotted at different scan rates, (c) Plot of anodic and cathodic as a function of $\upsilon^{1/2}$, (d) Plot of rate law (log I vs log υ) for the two redox couples, and Trasatti plots of (e) 1/q vs $\upsilon^{1/2}$ and (f) q vs $\upsilon^{-1/2}$.

Galvanostatic experiments were performed for a more accurate capacitance assessment of $NiC_2O_4 \cdot 2H_2O$ electrode samples. From the charge-discharge curve, the specific capacitance of the electrode can be calculated using equation 3.9: [23]

$$Csp = \frac{I\Delta t}{m\Delta V} \quad (3.9)$$

where I is the discharge current (A), Δt the discharge time (s), m is the mass of the active material in the electrode (g), and ΔV is the potential change during discharge (V). The specific capacitances of 838 F/g, 788 F/g, 750 F/g, 731 F/g, 713 F/g, and 650 F/g at current densities of 1, 1.5, 2, 2.5, 3 and 5 A/g respectively. It has been observed that with the increase in current density, there was a decrease in specific capacitance.

Figure 3.7(a) exhibits excellent long-term cycle stability of $NiC_2O_4 \cdot 2H_2O$ electrodes at 5 A/g for 2500 cycles. ~96% capacity of material retention was observed even after 2500cycle. Simultaneously, Figure 3.7(b) also displays the coulombic efficiency ($\eta = {}^{t_d}/_{t_c}$) of electrode equivalent to 99% after 2500 cycles of charge/discharge which reveals the high reversibility of the $NiC_2O_4 \cdot 2H_2O$ electrode. In addition to electrochemical stability, we performed EIS as shown in Figure 3.7(c) in the frequency range of 1–100 kHz at 10 mV applied potential. Figure 3.7(d) shows a comparative CV curve of different types of electrodes fabricated at nickel foam and carbon Toray paper in 2M KOH. The carbon Toray paper electrode showed superior diffusion control compared to the Nickel foam electrode. Figure 3.7(e) show the Comparative CV study in different concentration of electrolytes ranging from 1 M to 3 M. According to the study, redox potential is shifted to a lower value with increasing concentration of KOH electrolyte and is not desirable for high voltage supercapacitors applications. Further, current density values also confirmed the decrease in capacitance value above 2M KOH concentration.

The sloping curve from higher to lower frequency exhibits that diffusion control reaction at the surface of the $NiC_2O_4 \cdot 2H_2O$ electrode. [24] The curve reveals that internal resistance and charge transfer resistance before and after the cycles were not significantly changed. These results confirm that $NiC_2O_4 \cdot 2H_2O$ electrodes prepared for this study have high specific capacitance and excellent rate capabilities

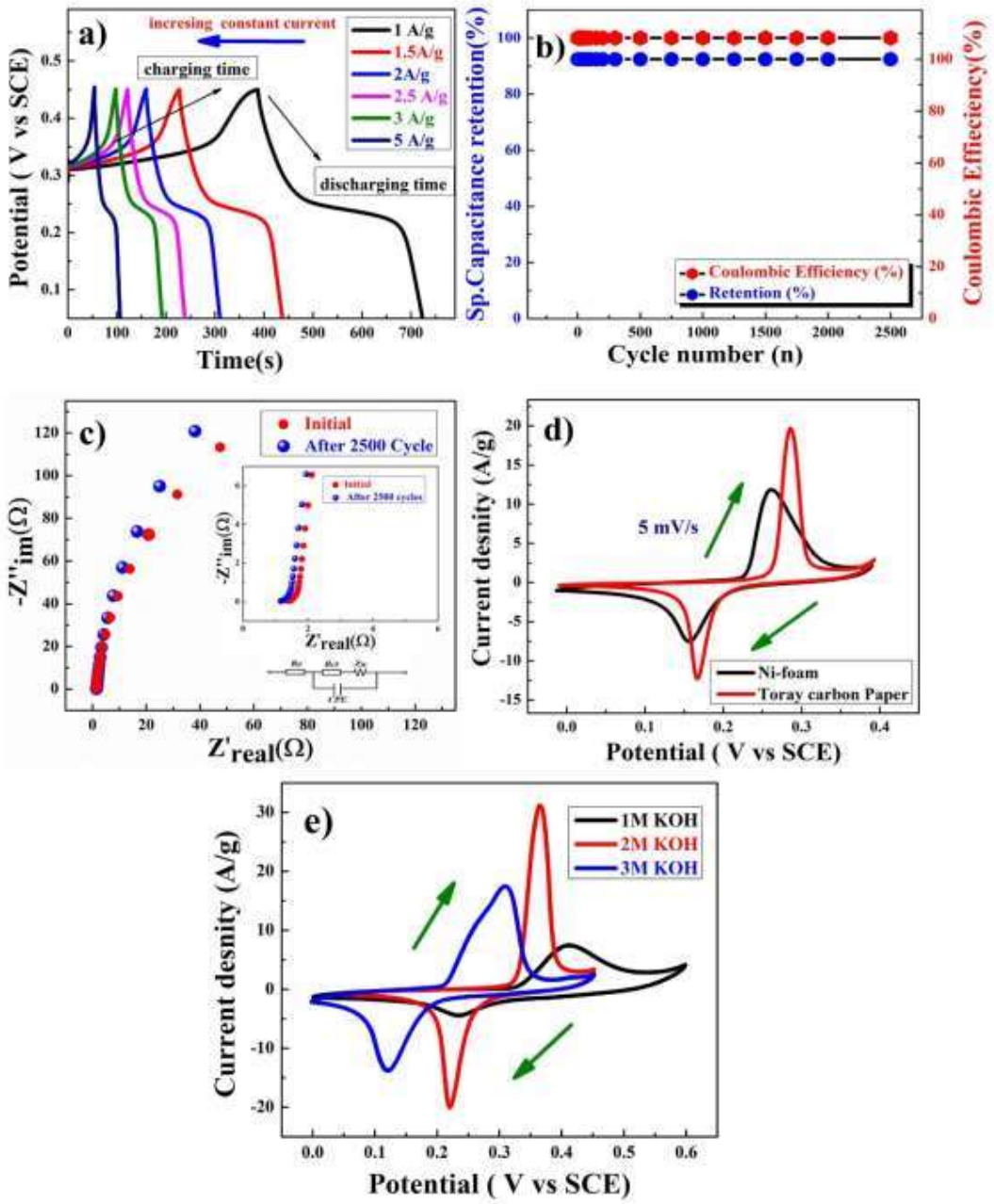

Figure 3.7 (a) Galvanostatic charge/discharge curve at different current densities (b) Cyclic stability graph at 5A/g for 2500 cycle and coulombic efficiency. (c) The plot of electrochemical impedance spectra (EIS) at 10mV applied potential. d) Compare CV plot in a different type of electrode nickel foam and carbon Toray paper in 2M KOH e) Compare CV study in different type electrolyte in 1M to 3M

Further, studies were conducted to understand the charge storage behavior of $NiC_2O_4•2H_2O$ electrodes in a 1 M Na_2SO_4 neutral electrolyte. The CV curve at various scan rates as shown in figure 3.8(a) indicates a redox peak into well-separated redox peaks at +0.52/+0.19 V. As specific capacitance is the function of scan rate has been estimated using equation (3.5) where 1M Na_2SO_4 electrolyte, the specific capacitance of 440 F/g, 310 F/g, 256 F/g, 215 F/g, 188 F/g, 170 F/g, and 147 F/g at 1mV/s, 5 mV/s, 10 mV/s, 20 mV/s, 30 mV/s, 50 mV/s, 100 mV/s respectively was observed for the $NiC_2O_4•2H_2O$ electrode. Subsequently, the quantitative galvanostatic charge/discharge storage measurement has been performed and the results are shown in Figure 3.8(b). The estimated value of specific capacitance in 1 M Na_2SO4 electrolyte was found to be 384 F/g, 220 F/g, 150 F/g, 100 F/g, 55 F/g at 0.5 A/g, 1 A/g, 2 A/g, 5 A/g, and 10 A/g respectively.

Moreover, a comparative study was conducted to analyze the effects of anions present in the electrolyte. Figure 3.8(c) shows the comparative CV curve of $NiC_2O_4•2H_2O$ electrodes in 2 M KOH and 1 M Na_2SO_4 electrolytes. Shifts in the redox peaks were observed from KOH to Na_2SO_4 electrolyte. Further, the redox peaks were also found to be more dominant in 2 M KOH compared to 1 M Na_2SO_4, this may be due to the size difference of hydration radii of sulfate ions (3.79 Å) as compared to hydroxyl ions (3 Å). A larger hydration sphere of SO_4^{2-} further leads to the decrement of ions entering the pores, causing lower electric double layer formation and slower diffusion. [25-26] In addition, in KOH electrolyte, $NiC_2O_4•2H_2O$ electrode exhibits higher current response in CV curve due to the superior molar conductivity OH^- ion (198 $cm^2\Omega\ mol^{-1}$) as compared to SO_4^{2-} (79.8 $cm^2\Omega\ mol^{-1}$) in Na_2SO_4 [12,26]. From the CV curve shape displayed in Figure3.8(c), it is evident that $NiC_2O_4•2H_2O$ electrodes display better Faradic redox characteristics in KOH electrolytes. Galvanostatic experiments were performed for determining the quantitative capacitance assessment of the electrode in 2 M KOH and 1 M Na_2SO_4 electrolytes. From figure 3.8(d) (see the discharge time), it is clear

that the electrode delivers a longer discharge time in 2 M KOH electrolyte as compared to 1 M Na_2SO_4 electrolyte at a 1 A/g current rate. Subsequently, comparisons of specific capacitance carried out at different current densities in both the electrolytes are shown in Figure 3.8(e). These studies confirm the suitability of aqueous 2 M KOH electrolyte for the high performance of the electrode as the smaller size of OH^- anions matches well with the pore diameter of the electrode resulting in superior performance

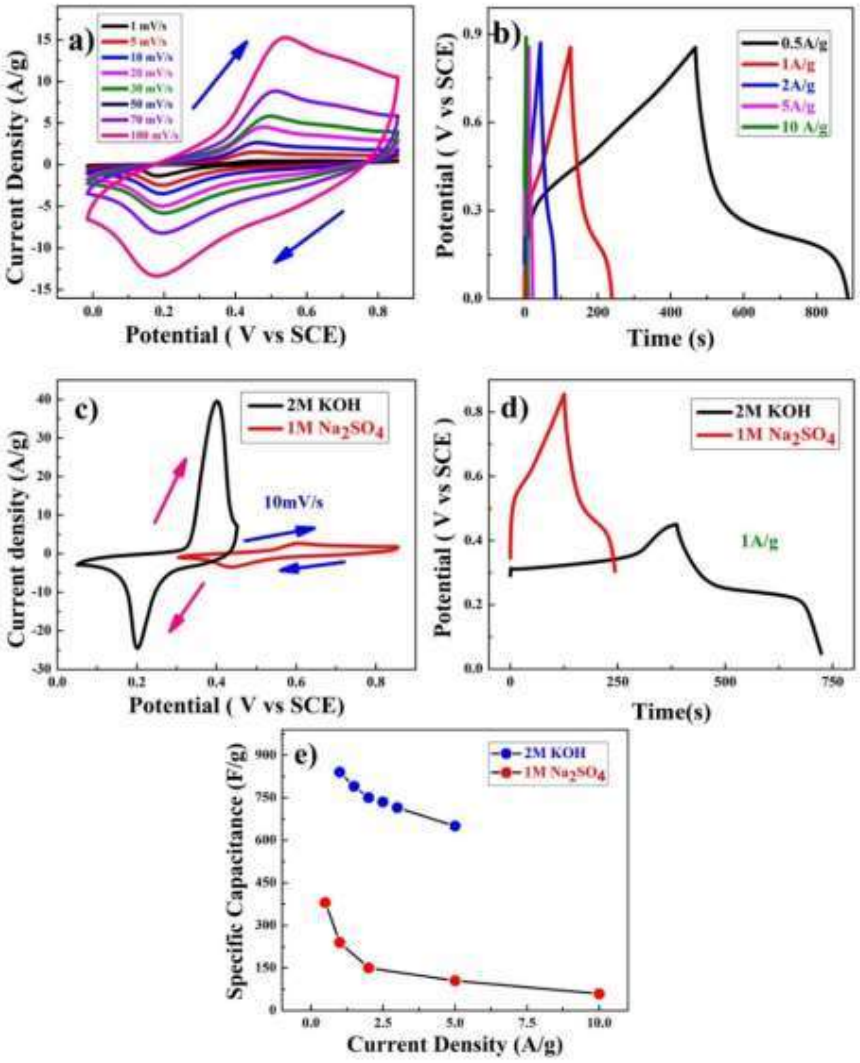

Figure 3.8: (a) CV and (b) Galvanostatic charge/discharge (GCD) curve of $NiC_2O_4 \cdot 2H_2O$ electrode in 1M Na_2SO_4 electrolyte. (c) Comparative CV diagram of $NiC_2O_4 \cdot 2H_2O$ in KOH and Na_2SO_4 medium at 10mV/s, (d) Comparative charge/discharge curve of $NiC_2O_4 \cdot 2H_2O$ in KOH and Na_2SO_4 medium at 1A/g, (e) Specific capacitance of $NiC_2O_4 \cdot 2H_2O$ electrode in KOH and Na_2SO_4 electrolyte at different current density.

To get a negative electrode for the fabrication of a full cell, further studies were made on activated carbon. Activated Carbon (AC) as a negative electrode was evaluated in a three-electrode system by CV, GCD, and EIS techniques in an aqueous 2 M KOH electrolyte solution. Figure 3.9 (a) depicts the CV curve for AC in the region -1 V to 0 V which shows the nature of storage of charge is only due to the electrical double layer (EDLC). With the increase in scan rate, the area under the CV curve also increases which signifies the storage of charge in AC is due to surface absorptions of ions. The charge/discharge curve in Figure 3.9(b) between -1 V and 0.0 V at different specific currents displays a perfectly triangular nature curve and confirms the electrical double layer behavior of AC. The specific capacitances obtained were 140 F/g, 110 F/g, 108 F/g, 101 F/g, 97 F/g, and 94 F/g at current densities of 0.5, 1, 2, 4, 5, and 10 A/g, respectively. From Figure 3.9(c), it can be concluded that the AC electrode offers good cycle life i.e. 98% retention after 3000 cycles at 2 A/g with excellent coulombic efficiency. At lower frequency, the vertical line which is nearly parallel to imaginary impedance resembles the EDLC nature of AC.[27] In addition to supporting the high cyclic stability of AC for 3000 cycles, EIS measurements at 10mV applied potential as shown in Figure 3.9(d) exhibits a negligible change in the resistance of the electrode.

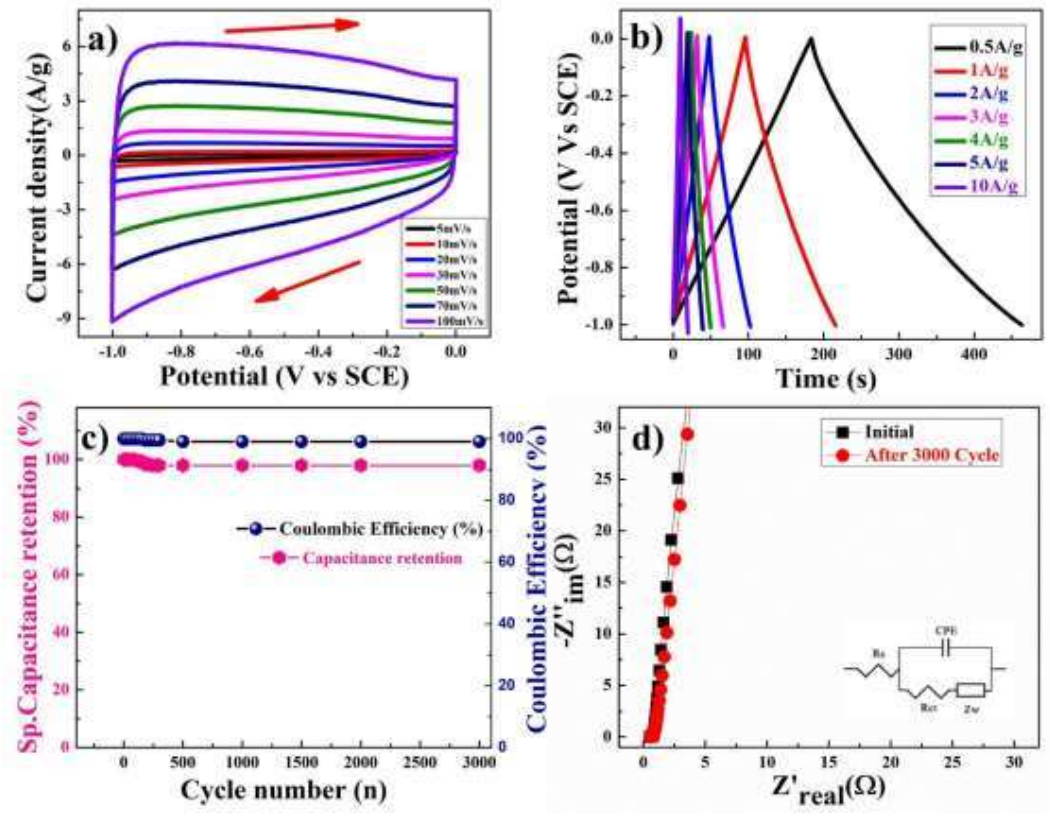

Figure 3.9: (a) CV curve at different scan rates, (b) Charge-discharge curve at various current densities (c), cyclic stability and coulombic efficiency at 2A/g, and (d) plot of electrochemical impedance test at 10mV applied Potential of Activated carbon.

3.3.5 Two electrode test

Two electrode measurements have been conducted in 2 M KOH, to understand the usable charge storage behavior of $NiC_2O_4 \cdot 2H_2O$ using AC as a counter electrode. To determine the maximum specific capacitance during the full test, the storage capacity of positive and negative electrodes needs to be balanced using equation 3.10:

$$\frac{1}{C_{total}} = \frac{1}{C_{positive}} + \frac{1}{C_{negative}} \qquad (3.10)$$

For balancing the charge storage capacity of the cell, the mass ratio (m^+/m^-) of positive and negative electrode material was measured using equation 3.11:

$$\frac{m^+}{m^-} = \frac{C_- \times \Delta E_-}{C_+ \times \Delta E_+} \quad (3.11)$$

$m^+, m^-, C_+, C_-, \Delta E_+, \Delta E_-$ are mass, specific capacitance, and potential window of positive and negative electrodes estimated by three-electrode measurements. The calculated mass ratio ($\frac{m^+}{m^-}$) was 1:1.4. For the asymmetric cell, the weight of the active material was 2.5 mg (excluding the weight of acetylene black and PVDF). Specific capacitance for a two-electrode system was calculated as $C_{total} = 4\, C_{sp}$. [27-29] Equation (3.5) was used to determine the C_{sp} of $NiC_2O_4 \cdot 2H_2O$ //AC full cell. Figure 3.10(a) demonstrates the CV curve of $NiC_2O_4 \cdot 2H_2O$ //AC AAS cell at different scan rates, ranging from 5 mV/s to 100 mV/s. Subsequently, the charge/discharge study shows the capacitance equivalent to 520 F/g, 277 F/g, 240 F/g, 228 F/g, 204 F/g, and 200 F/g at different current densities, i.e. 0.2 A/g,0.5 A/g, 0.8 A/g, 1 A/g, 1.5 A/g, and 2 A/g respectively as shown in Figure 3.10(b). $NiC_2O_4 \cdot 2H_2O$ //AC (AAS) cell shows brilliant cyclic stability with 96% capacity retention after 1500 cycles as shown in Figure 3.10(c). The coulombic efficiency of two-electrode cells has lost only 3% of its initial value after 1500 cycles. In addition, EIS measurement was also carried out with 10mV applied potential before and after completion of 1500 cycles at 2 A/g as shown in Figure 3.10(d). The EIS result supports the cyclic stability showing a slight change in internal and charge transfer resistance of the cell before and after the test. Specific energy and specific power of asymmetric capacitors were calculated using equations 3.12&3.13:

$$E = \frac{1}{2} C_{sp} V \quad (3.12)$$

$$P = \frac{E}{t_{dis}} \quad (3.13)$$

where C_{sp} is specific capacitance, V is operating voltage and t_{dis} is discharge time

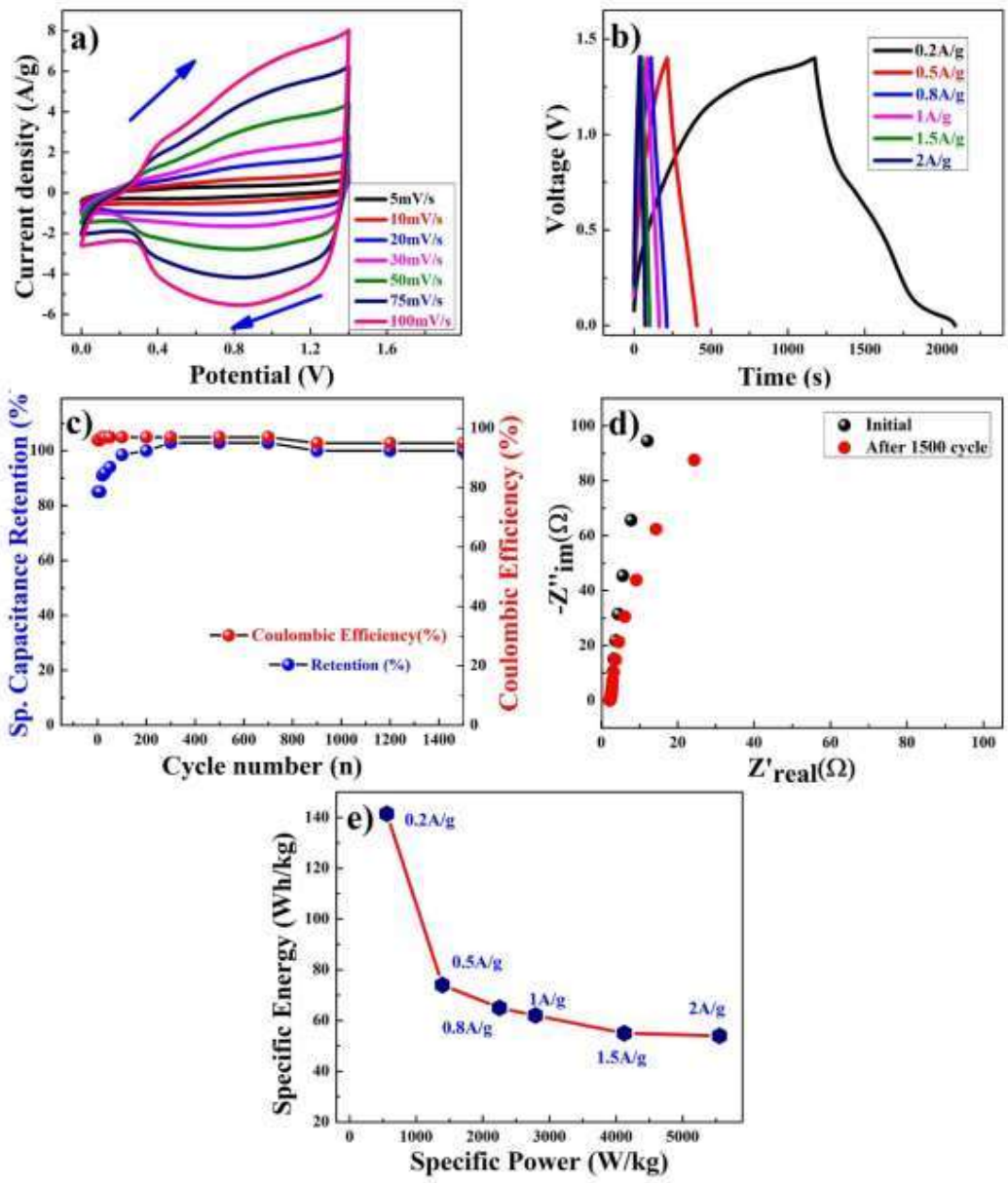

Figure 3.10: (a) CV and (b) GCD, (c) cyclic stability and Coulombic efficiency of AAS cell $NiC_2O_4•2H_2O$ //AC full cell. (d) The electrochemical impedance spectroscopy (EIS) analysis of as-prepared of $NiC_2O_4•2H_2O$ //AC full cell before and after 1500 cycles at 10 mV of applied potential. (e) Ragone plot of $NiC_2O_4•2H_2O$ //AC full cell showing specific energy vs. specific power.

The asymmetric cell shows the highest specific energy equivalent to 141.5 Wh/kg at 0.2 A/g current density and specific power of ~559 W/kg. Maximum specific power of ~5554 W/kg was obtained when specific energy was reduced to ~54 Wh/kg at 2 A/g of current density as shown in Figure 3.10(e). Table 3.1 shows the comparison of specific energy with $NiC_2O_4•2H_2O$ //AC cell as an asymmetric supercapacitor.[23,30-36].

Aqueous Asymmetric Capacitors (ASC)	Specific Energy (Wh/kg)	Ref.
$Ni_3V_2O_8$@MWCT//β-FeOOH	86.7	[23]
NiO//AC	36.5	[30]
Ni-$Ni(OH)_2$//AC	23.45	[31]
β-Ni/S//AC	42.12	[32]
H-$NiCo_2S_4$//AC	35.6	[33]
$Ni_3(PO)_4$GF//C-FP	49	[34]
$Co_{0.5}Ni_{0.5}C_2O_4$//AC	283	[35]
Anhydrous CoC_2O_4//AC	129	[36]
$NiC_2O_4•2H_2O$ //AC	141.5	This work

Table 3.1. Comparison of specific energy values for different reported Aqueous Asymmetric Nickel-based positive electrode supercapacitors

3.4 Conclusions

In summary, $NiC_2O_4•2H_2O$ flakes were synthesized using a single-step co-precipitation method in an aqueous medium. $NiC_2O_4•2H_2O$ based electrode showed intercalative charge storage behavior exhibiting specific capacitance of 990 F/g at a current density of 1 A/g with excellent cyclic stability. $NiC_2O_4•2H_2O$ electrode showed superior specific capacitance equivalent to 990 F/g in the potential window of 0.45 V was observed in an aqueous KOH electrolyte and 440 F/g in 1M neutral Na_2SO_4 electrolyte in the potential window of 0.85 V.

Predominant intercalative mechanism seems to be operative behind high charge storage as intercalative (Inner) and surface (outer) charges stored on $NiC_2O_4 \cdot 2H_2O$ electrodes were found to be 84% and 16% respectively. In 2 M KOH electrolyte, $NiC_2O_4 \cdot 2H_2O$ //AC full cell resulted in 141.5 Wh/kg of maximum specific energy with specific power equivalent to 559 W/kg in the voltage window of 1.4 V in 2 M KOH electrolyte at 0.2 A/g current density. These results confirm that $NiC_2O_4 \cdot 2H_2O$ can act as a potential pseudocapacitive electrode for large energy storage applications.

References:

1. V. Augustyn, P. Simon, B. Dunn, Pseudocapacitive oxide materials for high-rate electrochemical energy storage, Energy Environ. Sci. 2014, 7(5),1597–1614.
2. L. Y. Chen, Y. Hou, J. L. Kang, A. Hirata, M. W. Chen, Asymmetric metal oxide pseudocapacitors advanced by three-dimensional nanoporous metal electrodes, J. Mater. Chem. A 2014, 2, 8448–8455.
3. (a) J. S. Yeoh, C. F. Armer, A. Lowe, Transition metal oxalates as energy storage materials. A review, Mater. Today Energy 2018, 9, 198–222. (b) H. Wang, X. Zhao, L. Chen, Mater. Today Chemistry 2021, 22, 100564.
4. (a)S. Liang, H. Wang, Y. Li, H. Qin, Z. Luo, L.Chen, Ternary synergistic transition metal oxalate 2D porous thin sheets assembled by 3D nanoflake array with high performance for supercapattery, Applied Surface Science 2021, 567, 150809. (b) T. Pu, J. Li, Y. Jiang, B. Huang, W. Wang, C. Zhao, L. Xie, L. Chen, Size and crystallinity control of two-dimensional porous cobalt oxalate thin sheets: tuning surface structure with enhanced performance for aqueous asymmetric supercapacitors, Dalton Trans. 2018, 47, 9241–9249. (c) L. Chen, Q.Zhang, H. Xu, X. Hou, L. Xuan, Y. Jiang, Y.Yuan, Amorphous 3D nanoflake array-assembled porous 2D cobalt–oxalate coordination polymer thin sheets with excellent pseudocapacitive performance, J. Mater. Chem. A 2015, 3, 1847–1852.
5. E. J. Baran, Review: Natural oxalates and their analogous synthetic complexes, J. Coord. Chem. 2014, 67(23–24), 3734–3768.
6. F. Wang, S. Xiao, Y. Hou, C. Hu, L. Liu, Y. Wu, Electrode materials for aqueous asymmetric supercapacitors, RSC Adv. 2013, 3(32), 13059–13084.
7. A. N. Puzan, V. N. Baumer, D. V. Lisovytskiy, P. V. Mateychenko, Structure transformations in nickel oxalate dihydrate $NiC_2O_4 \cdot 2H_2O$ and nickel formate

dihydrate $Ni(HCO_2)_2 \cdot 2H_2O$ during thermal decomposition, J. Solid State Chem. 2018, 266, 133–142.

8. H. -J. Oh, C.-H. Jo, C. S. Yoon, H. Yashiro, S.-J. Kim, S. Passerini, Y.-K. Sun, S.-T. Myung, Nickel oxalate dihydrate nanorods attached to reduced graphene oxide sheets as a high-capacity anode for rechargeable lithium batteries, NPG Asia Mater. 2016, 8(5), e270.
9. A. Angermann, J. Töpfer, Synthesis of nanocrystalline Mn–Zn ferrite powders through thermolysis of mixed oxalates, Ceram. Int. 2011, 37(3), 995–1002.
10. M. Salavati-Niasari, N. Mir, F. Davar, Synthesis and characterization of NiO nanoclusters via thermal decomposition, Polyhedron 2009, 28(6), 111–1114.
11. F. Behnoudnia, H. Dehghani, Anion effect on the control of morphology for NiC2O4·2H2O nanostructures as precursors for synthesis of $Ni(OH)_2$ and NiO nanostructures and their application for removing heavy metal ions of cadmium(II) and lead(II). Dalt. Trans. 2014, 43(9), 3471–3478.
12. L. An, Q. Ren, W. Li, K. Xu, Y. Cao, T. Ji, R.Zou, Z. Chen, J. Hu, Highly Ordered Mesoporous NiCo2O4 with Superior Pseudocapacitance Performance for Supercapacitors, J. Mater. Chem. A 2015, 3(21), 11503–11510.
13. F. Barzegar, D. Y. Momodu, O. O. Fashedemi, A. Bello, J. K. Dangbegnon, N. Manyala, Investigation of different aqueous electrolytes on the electrochemical performance of activated carbon-based supercapacitors, RSC Adv. 2015, 5 (130), 107482–107487.
14. R. Sahoo, D. T.Pham, T. H. Lee, T. H. Thuong Luu, J. Seok, Y. H. Lee, Redox-Driven Route for Widening Voltage Window in Asymmetric Supercapacitor, ACS nano 2018, 12(8), 8494–8505.
15. H. B. Li, M. H. Yu, F. X. Wang, P. Liu, Y. Liang, J. Xiao, C. X. Wang, Y. X. Tong,

G. W. Yang., Amorphous nickel hydroxide nanospheres with ultrahigh capacitance and energy density as electrochemical pseudocapacitor materials, Nature Communications. 2013, 4, 1894.

16. S. Rudra, R. Chakraborty, P. K. Maji, S. Koley, A. K. Nayak, D. Paul, M. Pradhan, Intercalation pseudocapacitance in chemically stable Au-α-Fe_2O_3-Mn_3O_4 composite nanorod: Towards highly efficient solid-state symmetric supercapacitor device, Electrochim. Acta 2019, 324, 134865.
17. B. Ramkumar, S. Yuvaraj, S. Surendran, K. Pandi,, H. V. Ramasamy, Y. S. Lee, R. K. Selvan, Synthesis and characterization of carbon coated $LiCo_{1/3}Ni_{1/3}Mn_{1/3}O_2$ and bio-mass derived graphene like porous carbon electrodes for aqueous Li-ion hybrid supercapacitor, J. Phys. Chem. Solids 2018, 112, 270-279.
18. N. Mayedwa, N. Mongwaketsi, S. Khamlich, K. Kaviyarasu, N. Matinise, M. Maaza, Green synthesis of zin tin oxide ($ZnSnO_3$) nanoparticles using Aspalathus Linearis natural extracts: Structural, morphological, optical and electrochemistry study, Appl. Surf. Sci. 2018, 446, 250-257.
19. D. Su, A. McDonagh, S. Z. Qiao, G. Wang, High-Capacity Aqueous Potassium-Ion Batteries for Large-Scale Energy Storage, Adv. Mater. 2017, 29(1), 1–8.
20. V. Augustyn, J.Come, M. A. Lowe, J. W. Kim, P.-L. Taberna, S. H. Tolbert, H. D. Abruña, P. Simon, B. Dunn, High-rate electrochemical energy storage through Li^+ intercalation pseudocapacitance, Nat. Mater. 2013, 12, 518–522.
21. M. Verma, R. Yadav, L. Sinha, S. S. Mali, C. K. Hong, P. M. Shirage, Pseudocapacitive-battery-like behavior of cobalt manganese nickel sulfide (CoMnNiS) nanosheets grown on Ni-foam by electrodeposition for realizing high capacity, RSC Adv. 2018, 8(70), 40198–40209.
22. W. Ren, X. Chen, C. Zhao, Ultrafast Aqueous Potassium-Ion Batteries Cathode for

Stable Intermittent Grid-Scale Energy Storage, Adv. Energy Mater. 2018, 8(24), 1–8.

23. R. Sahoo,T. Pal, Proportion of composition in a composite does matter for advanced supercapacitor behaviorJ. Mater. Chem. A 2016, 4, 17440-17454.
24. K. J. Samdani, J. H. Park, D. W. Joh, K. T. Lee, Self-Assembled Bi_2MoO_6 Nanopetal Array on Carbon Spheres toward Enhanced Supercapacitor Performance, ACS Sustain. Chem. Eng. 2018, 6, 16702–16712.
25. A. Ang, N. Gupta, R. Prasanth, S. Madhavi, High-performing mesoporous iron oxalate anodes for lithium-ion batteries, ACS Appl. Mater. Interfaces 2012, 4(12), 7011–7019.
26. B. Pal, S. Yang, S. Ramesh, V. Thangadurai, R. Jose, Electrolyte selection for supercapacitive devices: a critical review, Nanoscale Adv. 2019, 1(10), 3807–3835.
27. T. S. Mathis, N. Kurra, X. Wang, D. Pinto, P. Simon, Y. Gogotsi, Energy Storage Data Reporting in Perspective—Guidelines for Interpreting the Performance of Electrochemical Energy Storage Systems, Adv. Energy Mater.2019, 9(39), 1902007(1-13).
28. R. Sahoo, A. K. Sasmal, C. Ray, S. Dutta, A. Pal, T. Pal, Suitable Morphology Makes $CoSn(OH)_6$ Nanostructure a Superior Electrochemical Pseudocapacitor, ACS Appl. Mater. Interfaces 2016, 8(28), 17987–17998.
29. K. Subramani, N. Sudhan, R. Divya, M. Sathish, All-solid-state asymmetric supercapacitors based on cobalt hexacyanoferrate-derived CoS and activated carbon, RSC Adv. 2017, 7(11), 6648–6659.
30. G. Cheng, Q. Bai, C. Si, W. Yang, C. Dong, H. Wang, Y. Gao, Z. Zhang., Nickel oxide nanopetal-decorated 3D nickel network with enhanced pseudocapacitive properties, RSC Adv. 2015, 5(20), 15042–15051.
31. S. R. Ede, S. Anantharaj, K. T. Kumaran, S. Mishra, S. Kundu, One step synthesis of

$Ni/Ni(OH)_2$ nano sheets (NSs) and their application in asymmetric supercapacitors, RSC Adv. 2017, 7(10), 5898–5911.

32. Y. Zhang, J. Zhang, D. Ding, Y. Gao, Controllable Synthesis of Three-Dimensional β-NiS Nanostructured Assembly for Hybrid-Type Asymmetric Supercapacitors, Nanomaterials 2020, 10(3), 2020, 487.
33. Y. Wen, S. Peng, Z. Wang, J. Hao, T. Qin, S. Lu, J. Zhang, D. He, X. Fan, G. Cao, J. Mater. Chem. A 2017, 5(15), 7144–7152.
34. A. A. Mirghni, M. J. Madito, K. O. Oyedotun, T. M. Masikhwa, N. M. Ndiaye, S. J. Ray, N. Manyala, Facile synthesis of ultrathin $NiCo_2S_4$ nano-petals inspired by blooming buds for high-performance supercapacitors, RSC Adv. 2018, 8(21), 11608–11621.
35. N. K. Mishra, R. Mondal, T. Maiyalagan, P. Singh, Synthesis, Characterizations, and Electrochemical Performances of Highly Porous, Anhydrous $Co_{0.5}Ni_{0.5}C_2O_4$ for Pseudocapacitive Energy Storage Applications, ACS Omega 2022, 7(2), 1975–1987.
36. N. K. Mishra, R. Mondal, P. Singh, Synthesis, characterizations and electrochemical performances of anhydrous CoC_2O_4 nanorods for pseudocapacitive energy storage applications, RSC Adv. 2021, 11, 33926–33937.